PHYSICAL REVIEW MATERIALS **3**, 041201(R) (2019)

**Rapid Communications**

# Fermi surface of the flat-band intermetallics $A\mathrm{Pd}_3$ ($A = \mathrm{Pb},\ \mathrm{Sn}$)

Kaya Wei,[1,*] Kuan-Wen Chen,[1,2] Jennifer N. Neu,[1,2] You Lai,[1,2] Greta L. Chappell,[1,2] George S. Nolas,[3] David E. Graf,[1] Yan Xin,[1] Luis Balicas,[1,2] Ryan E. Baumbach,[1,2] and Theo Siegrist[1,4]
[1]*National High Magnetic Field Laboratory, Florida State University, Tallahassee, Florida 32310, USA*
[2]*Department of Physics, Florida State University, Tallahassee, Florida 32306, USA*
[3]*Department of Physics, University of South Florida, Tampa, Florida 33620, USA*
[4]*Department of Chemical and Biomedical Engineering, FAMU-FSU College of Engineering, Tallahassee, Florida 32310, USA*

(Received 18 February 2019; published 3 April 2019)

The intermetallic phases $A\mathrm{Pd}_3$ ($A = \mathrm{Pb},\ \mathrm{Sn}$) were recently predicted to host an unconventional combination of unique electronic structure features, namely, flat bands near the Fermi energy coexisting with topologically protected surface states at the Γ point. These features each could independently produce alternative electronic states, including electronically or magnetically ordered states coexisting with unconventional edge dominated transport and a significantly large thermopower coexisting with topological characteristics. To investigate these expectations, we report the synthesis, structural/chemical characterization, electrical and thermal transport properties, magnetic torque (up to 45 T), and Fermi surface mapping for single crystals produced using the Czochralski technique. X-ray diffraction and scanning transmission electron microscope measurements establish the absence of defects, while small measured values of the thermopower indicate that the Fermi level is located away from the flat-band region. The electronic properties are further clarified by the topography of the Fermi surfaces, measured through the de Haas–van Alphen effect. We find that the Fermi levels are placed at higher energy values than the original ones resulting from the density functional theory calculations, 54 meV higher for $\mathrm{PbPd}_3$ and 68 meV higher for $\mathrm{SnPd}_3$. The molten flux method was also used to synthesize $\mathrm{PbPd}_3$, yielding nearly identical Fermi surfaces between the specimens grown using different synthesis techniques, indicating the robustness of the Fermi level position. According to the density functional theory calculations, the flat band is mainly formed by the 4*d* bands of Pd. Therefore, we propose monovalent doping on the Pb/Sn site as a viable approach to accessing the flat band while maintaining the unique band structure features of these compounds.

DOI: 10.1103/PhysRevMaterials.3.041201

In recent years there have been far reaching efforts to search for three-dimensional topological semimetals, which offer a chance to explore topological matter through an approach that is separate from topological insulators. Among these materials, the compounds $A\mathrm{Pd}_3$ ($A = \mathrm{Pb},\ \mathrm{Sn}$) were identified as candidate materials where the density functional theory (DFT) based methods reveal (i) a dispersionless band along the Γ-*X* line lying closely to the Fermi level ($E_\mathrm{F}$); (ii) triple nodal points and three-dimensional nodal loops in the absence of spin-orbit coupling (SOC); (iii) Fermi arcs and Dirac surface states presenting clearly within the Perdew-Burke-Ernzerhof generalized gradient approximation (GGA) + SOC; and (iv) topological characteristics on the $k_z = 0$ plane [1]. Exotic physical properties are expected due to these fascinating features. For instance, the unconventional surface state might enable topological protection, making these compounds potential candidates for applications involving topological matter [2–4]. In addition, the large electronic density of states (DOS) of the flat band may promote alternative bulk electronic properties such as an enhanced Seebeck coefficient (thermopower) or superconductivity [5–10]. A very recent study also suggests a large transverse magnetoresistance in $\mathrm{PbPd}_3$, 650% at 1.8 K under 14 T [11].

In this study, we synthesized large single crystals of $\mathrm{PbPd}_3$ and $\mathrm{SnPd}_3$ by the Czochralski technique. The crystal structure and Pb(Sn) – Pd site ordering were characterized using both x-ray diffraction (XRD) and scanning transmission electron microscopy (STEM) which reveal negligible chemical or site disorder. The thermoelectric properties and magnetic torque (up to 45 T) were measured for both compounds. The geometry of the Fermi surfaces was revealed through the de Haas–van Alphen (dHvA) effect which was detected in the magnetic torque. In order to further verify these results, $\mathrm{PbPd}_3$ was also synthesized using a Pb flux method, where we find the angular dependence of the dHvA oscillations to be nearly identical to that of the samples grown using the Czochralski process. By comparison with the DFT calculations, we conclude that the Fermi surface features revealed by dHvA oscillations indicate the $E_\mathrm{F}$ to be placed at higher energies than the values calculated by DFT [1]: $\Delta E_\mathrm{F} = 54$ meV and 68 meV for $\mathrm{PbPd}_3$ and $\mathrm{SnPd}_3$, respectively. This result is supported by the small Seebeck coefficient values which indicate that the $E_\mathrm{F}$ is displaced away from the flat band. We propose strategies to tune $E_\mathrm{F}$ with a focus on maintaining the flat-band feature while placing $E_\mathrm{F}$ near the surface state or the bulk state.

Single crystals of $A\mathrm{Pd}_3$ were obtained through Czochralski process [Figs. 1(a) and 1(b)]. During both growths, the melts were prepared by melting the pure elements using induction heating in W crucibles in a ratio of $A : \mathrm{Pd} = 1 : 3$ and

---

[*] Corresponding author: kwei@magnet.fsu.edu

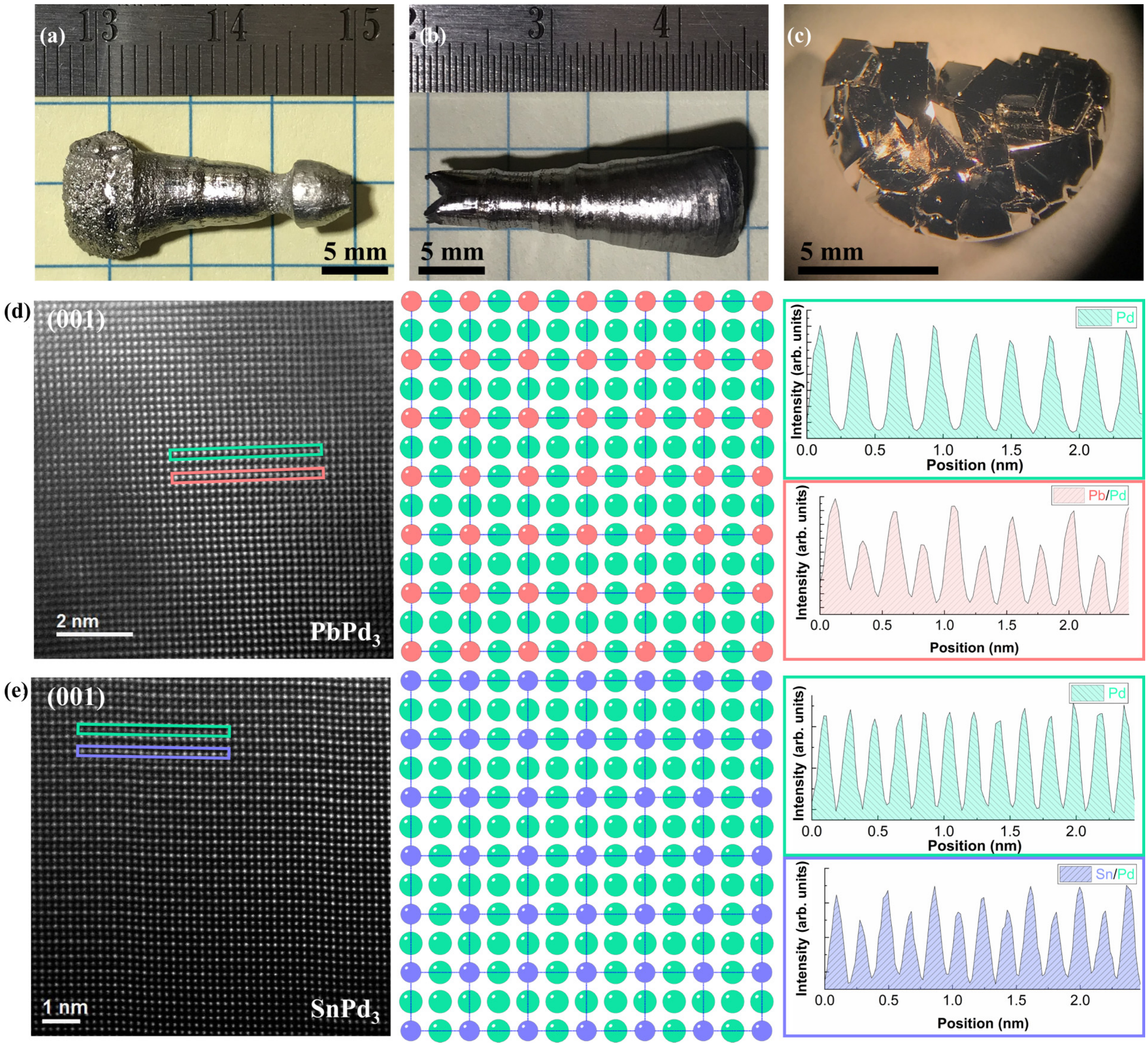

FIG. 1. Pictures of Czochralski-grown crystals: (a) $PbPd_3$, (b) $SnPd_3$, and (c) flux-grown $PbPd_3$. HAADF-STEM images of Czochralski-grown (d) $PbPd_3$ and (e) $SnPd_3$ are both shown in ⟨001⟩ projection with EDS line scan included.

pulling at a speed of 5 mm/h under 1200 °C and 1350 °C for $PbPd_3$ and $SnPd_3$, respectively. The as-synthesized crystals were sealed under vacuum in quartz tubes and annealed at 800 °C and 950 °C for $PbPd_3$ and $SnPd_3$, respectively, for 30 days to release any strain formed during the Czochralski process and ensure Pb(Sn) – Pd order. A molten Pb flux was also used to synthesize $PbPd_3$ single crystals. Elemental Pb and Pd were loaded into a 2-ml alumina crucible with the ratio of $\mathrm{Pb:Pd} = 1:20$ and sealed under vacuum within a quartz tube. These mixtures were heated at a rate of 50 °C/h to 1100 °C, held at this temperature for 1 day, and slowly cooled at a rate of 2 °C/h to 500 °C. The obtained crystals were subsequently centrifuged to separate them from the molten Pb flux. A Scintag PAD-V $\Theta/2\Theta$ reflection powder diffractometer (with line focus Cu $K\alpha$ beam and graphite analyzer together with a scintillator detector) and a custom-built diffractometer system (Rigaku rotating anode Cu $K\alpha$ source, graphite monochromatized in nondispersive geometry for high signal/noise ratio) were used to check the crystal structure, phase purity, and site ordering of the crystals.

Samples were prepared for TEM measurements by crushing the crystals in ethanol with a mortar and pestle. The suspension of crushed crystals was then dropped onto a 200-μm-mesh carbon/Formvar film TEM copper grid with a pipet. Samples prepared this way preserved the pristine and original quality of the crystals. The high-angle-annular-dark-field STEM (HAADF STEM) study was carried out using a probe-aberration-corrected, cold-field-emission JEM JEOL-ARM200cF at 200 kV using a JEOL HAADF STEM detector. The STEM imaging resolution is 0.078 nm. HAADF-STEM images were acquired using a 30-μm condenser lens aperture, at a camera length of 8 cm corresponding to a collection angle of 58.7 mrad, and an image scan speed of 32 $\mu$s/pixel. The beam convergent angle was 21 mrad.

Single crystals of $A\mathrm{Pd}_3$ were aligned using an Enraf-Nonius CAD-4 diffractometer along their [100] axis before being cut into a rectangular slab of 2 mm × 2 mm × 5 mm

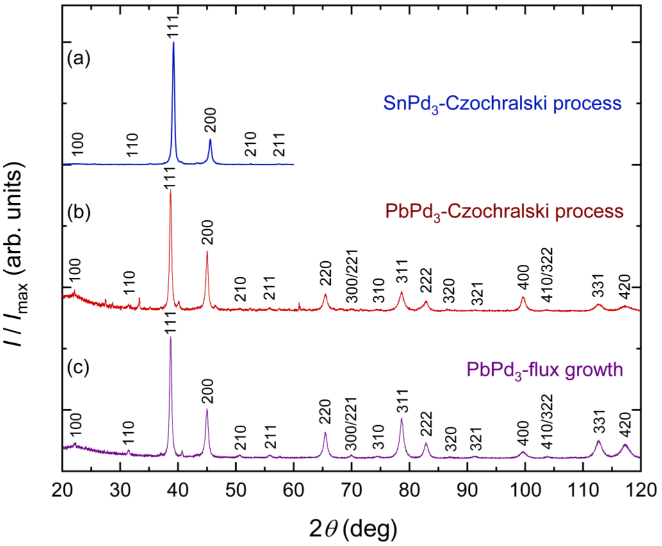

FIG. 2. Indexed powder XRD patterns of (a) $SnPd_3$ and (b) $PbPd_3$ grown through the Czochralski process and (c) $PbPd_3$ grown through molten flux. (a) $SnPd_3$ pattern was acquired using a high signal/noise custom-built x-ray system due to the weak superstructure intensities; (b,c) were collected using a Scintag PAD-V diffractometer.

dimensions for temperature-dependent four-probe electrical resistivity $\rho$, Seebeck coefficient $S$ (gradient sweep method), and steady-state thermal conductivity $\kappa$ measurements in the temperature range from 12 to 300 K. The crystals were mounted such that the current and the thermal gradient were both applied along the [100] direction. All the surfaces were polished using 3-μm-grit diamond polishing paper to reduce surface radiation losses during the measurements. The measurements were performed in a custom radiation-shielded vacuum probe with uncertainties of 4%, 6%, and 8% for $\rho$, $S$, and $\kappa$ measurements, respectively [12]. Electrical contacts to the specimens were made using silver epoxy and thermal contacts were made using Stycast epoxy. The magnetic torque $\tau$ was measured using a piezoelectric cantilever (SEIKO-PRC400) in the 45-T hybrid magnet at the National High Magnetic Field Laboratory in Tallahassee, FL.

DFT calculations were performed using the WIEN2K [13] implementation. We used the full-potential linearized augmented plane-wave method with the Perdew-Burke-Ernzerhof parametrization of the generalized gradient approximation (GGA PBE) [14]. The Brillouin zone was sampled by a dense $k$ mesh $40 \times 40 \times 40$ and the basis set cutoff $R_{\mathrm{mt}}K_{\max} = 9$, following the same condition as in [1]. SOC was included in all of our calculations. The angular dependencies of the oscillatory frequencies associated with each Fermi-surface cross-sectional area were computed through defining Supercell K-space Extremal Area Finder (SKEAF) code [15].

The as-synthesized crystals are shown in Figs. 1(a)–1(c). The Czochralski technique yields single crystals 23–25 mm in length. After annealing, the surface of the Czochralski-grown crystals began to show faceting parallel to the pulling direction and around the quasicylindrical body of the crystals. For the flux-grown $PbPd_3$, cubic-shape crystals with well-defined surfaces were obtained after removing the flux through centrifuging at elevated temperatures. We checked multiple Czochralski-grown crystals using STEM and did not observe disorder at the atomic resolution levels of the microscope [Figs. 1(d) and 1(e)]. Energy dispersive spectroscopy (EDS) confirmed that the stoichiometry was uniformly 1:3 in $APd_3$. In another approach to rule out the presence of disorders/vacancies in the specimens, we ground the crystals into fine powder and analyzed the powder XRD patterns with a focus on the $A$-Pd site occupancy preference (Fig. 2). We confirmed that indeed all of our samples crystallized in the cubic $Cu_3Au$-type structure [$Pm\bar{3}m$, space group 221, $a =$ 4.0357(8) and 3.9759(7) for $PbPd_3$ and $SnPd_3$, respectively] with full preferred site occupancy. The fact that the (100), (110), and (210) reflections are clearly observed is strong evidence of site ordering since the mixed site occupancy leads to an apparent higher-symmetry structure ($Fm\bar{3}m$, space group 225) with the reflections listed above as unobserved. Furthermore, using these reflections we estimate the ordering parameters to be close to 1 for the Czochralski-grown $SnPd_3$, the Czochralski-grown $PbPd_3$, and the flux-grown

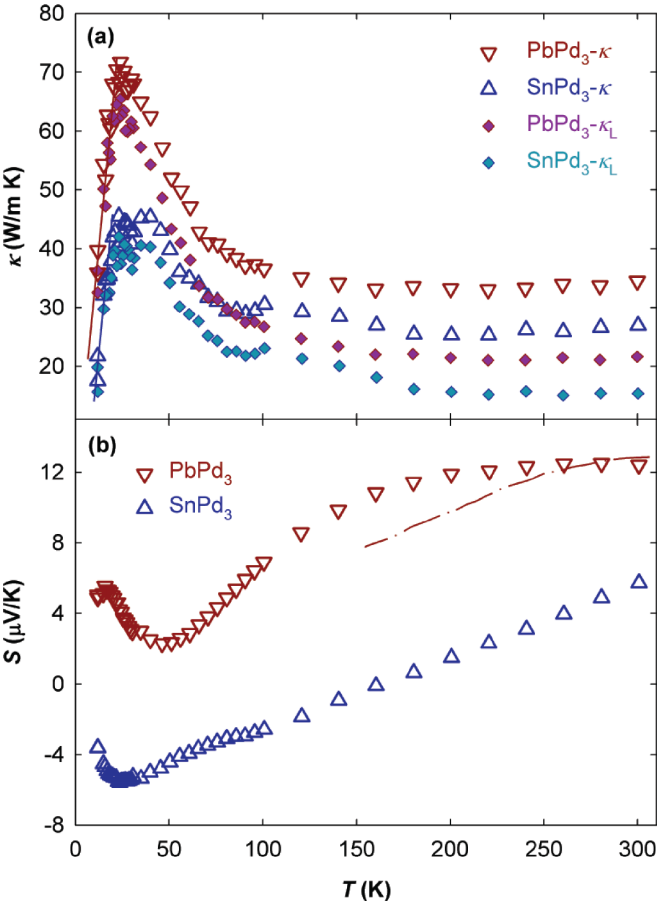

FIG. 3. Temperature dependence of (a) the thermal conductivity $\kappa$ and (b) the Seebeck coefficient $S$ of $PbPd_3$ (dark red triangles) and $SnPd_3$ (dark blue triangles). The solid diamond-shape dots depict the lattice contribution to the thermal conductivity, $\kappa_L$, of $PbPd_3$ (violet diamonds) and $SnPd_3$ (blue diamonds). The solid lines in (a) represent the $T^3$ temperature dependence. The dash-dot line in (b) is the calculated temperature-dependent Seebeck coefficient of $Pb_{0.97}Bi_{0.03}Pd_3$ from Ref. [1].

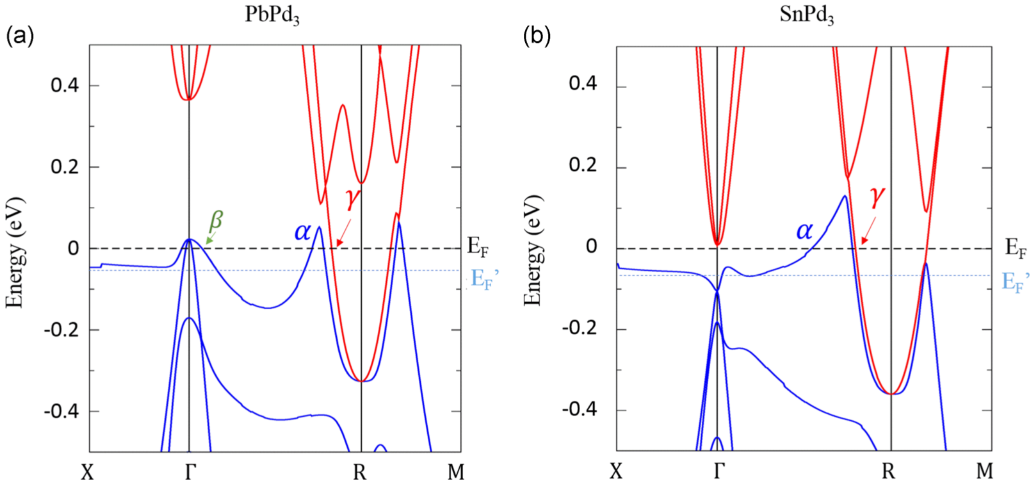

FIG. 4. Calculated band structures of (a) $PbPd_3$ and (b) $SnPd_3$. The Fermi level $E_F'$ is the value directly obtained from the DFT calculations, which is consistent with Ref. [1]. $E_F$ is the shifted Fermi level based on the experimental quantum oscillation data. $E_F - E_F' = 54$ meV for $PbPd_3$ and $E_F - E_F' = 68$ meV for $SnPd_3$. Flat bands along the $X$-Γ lines and the Fermi surface cross-sectional areas associated with the $\alpha$, $\beta$, and $\gamma$ dHvA orbits are indicated by arrows.

$PbPd_3$. We note that the magnetic torque and the transport properties measurements that will be described below were performed on the crystals grown through the Czochralski process.

DFT calculations predict that the $E_F$ is located at the flat band. This leads to the expectation that there should be a significant derivative $dN(E)/dE$ in the DOS at $E_F$. As a result, the Seebeck coefficient is expected to show a large value, making these materials interesting for thermoelectric applications. We therefore investigated the thermoelectric properties of $APd_3$ (Fig. 3 and Fig. S1 in the Supplemental Material [16]). Figure 3(a) shows $\kappa$ and the lattice contribution to $\kappa$ ($\kappa_L$) of $APd_3$ from 12 to 300 K. Employing the Wiedemann-Franz relation, the electronic thermal conductivity, $\kappa_E$, can be estimated from the relationship $\kappa_E = L_0\sigma T$ with the Lorenz number, $L_0 = 2.45 \times 10^{-8}\ V^2\,K^{-2}$ [17]. Thus, $\kappa_L$ can be estimated from $\kappa$–$\kappa_E$. At low temperatures, the phonon mean free path is limited by grain boundaries, which in this case corresponds to the size of the measured single crystal. The solid lines in Fig. 3(a) represent the $T^3$ temperature dependence of $\kappa_L$ which agree well with the measured data, indicating predominant boundary scattering of phonons [17]. $S(T)$ for $APd_3$ are shown in Fig. 3(b). As the temperature decreases, the Seebeck coefficients of both $PbPd_3$ and $SnPd_3$ decrease accordingly. The Seebeck coefficient of $SnPd_3$ changes from positive to negative around 160 K, and the curvatures in the $S(T)$ data indicate the competition between electrons and holes at the $E_F$. This corroborates the previously projected Fermi surface [1] and our Fermi surface mapping (to be discussed later) in which both electron- and hole pockets were observed. The absolute values of the Seebeck coefficient, on the other hand, suggest that the $E_F$ is placed away from the flat band. In fact, while the predicted $E_F$ of $PbPd_3$ lies near the flat band, by varying the electron concentration through Bi doping on the Pb site, the $E_F$, as well as the corresponding Seebeck coefficient, of $(Pb_{1-x}Bi_x)Pd_3$ were calculated for $x = 0.01,\ 0.02,\ 0.03$, and 0.033 [1]. We note that our measured Seebeck coefficient would be equivalent to that of the 3% doping which corresponds to an $E_F$ about 54 meV higher than the DFT prediction. We plotted the calculated Seebeck coefficient of 3% Bi-doped $PbPd_3$ together with our measured data as a comparison [dash-dot line in Fig. 3(b)].

Figure 4 shows the electronic band structures of $APd_3$. Based on our DFT calculations and previously reported results [1], a dispersionless flat band exists along the Γ-$X$ direction for both compounds. The band gaps of the bulk states at the Γ point are about 0.4 eV for $PbPd_3$ and 0.1 eV for $SnPd_3$. Together with the observed nontrivial surface states, our results agree with these predictions in Ref. [1]. Furthermore, for both $PbPd_3$ and $SnPd_3$, there are ellipsoidal-shaped hole pockets ($\alpha$ pockets) along Γ-$R$ and large, nearly spherical electron pockets near the $R$ point, as shown in Figs. 5(a) and 5(b). The cubic $\beta$ hole pocket near the Γ point, however, only appears in $PbPd_3$. We attribute this to the fact that the $E_F$ of $SnPd_3$ is located within the gap at the Γ point. While the $E_F'$ is calculated directly from DFT, which is consistent with Ref. [1], $E_F$ is the shifted Fermi level based on the experimental quantum oscillations data (discussed below). We note that both $E_F$'s measured by our dHvA oscillations are higher than those predicted from previous DFT calculations; $\Delta E_F = 54$ meV and 68 meV for $PbPd_3$ and $SnPd_3$, respectively. The differences are within the error bars inherent to DFT which is often seen in studies involving both DFT calculations and experimental approaches in terms of band structure determination. While it is generally acknowledged that uncertainties exist in exactly pinpointing the $E_F$ using different implementations of DFT, our $E_F$ for $PbPd_3$, as revealed from the dHvA oscillations, along with the measured Seebeck coefficient values appears to be equivalent to that of the 3% Bi-doped $PbPd_3$ in Ref. [1].

Torque magnetometry measurements are ideal to construct the Fermi surface via the dHvA effect. Due to an external magnetic field $\mu_0 H$, the cyclotron orbit becomes quantized and with increasing the field the separation in energy between Landau levels rises accordingly. Therefore, DOS is modulated periodically as a function of the inverse of the induction field $B$ as the Landau levels cross and leave the chemical potential,

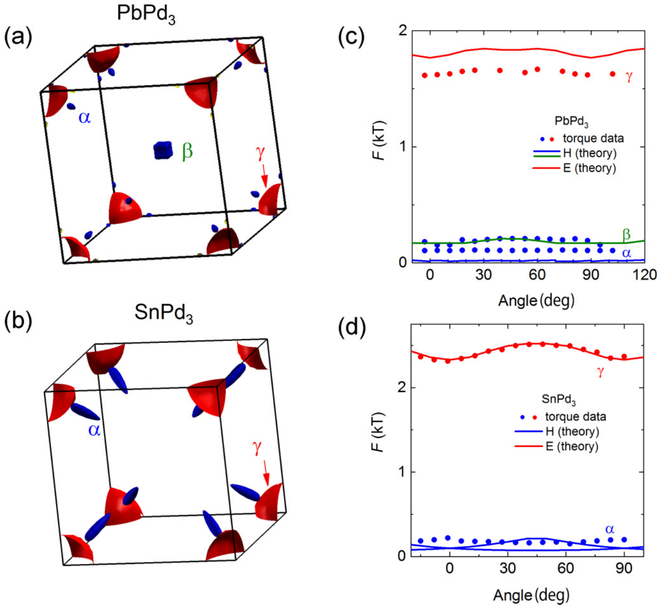

FIG. 5. Fermi surfaces for the shifted Fermi level $E_F$: (a) PbPd$_3$ and (b) SnPd$_3$. Hole- and electronlike pockets are depicted in blue and in red, respectively. The $\alpha$ orbit can be associated to an ellipsoidal hole pocket and the $\gamma$ orbit to a large, nearly spherical electron pocket. The cubic $\beta$ pocket near the Γ point only appears in PbPd$_3$. (c,d) show the cyclotron frequencies $F$ as a function of the angle $\theta$ relative to the crystallographic [001] axis.

according to the Lifshitz-Onsager quantization rule,

$$\frac{1}{B_n} = \frac{2\pi e}{\hbar}[n+\gamma]\frac{1}{A}, \quad (n = 0,\ 1,\ 2\cdots),$$

where $A$ is the extremal cross-sectional area of the Fermi surface normal to $B$, $e$ is the electron charge, $\bar{h}$ is Planck's constant, and $\Upsilon$ is the Onsager phase. The oscillatory dHvA signal was isolated by subtracting a smooth polynomial background from $\tau(B)$. The frequencies $F$ were then identified by using a fast Fourier transform [Figs. 5(c) and 5(d)]. The topography of the Fermi surface revealed by the quantum oscillations is consistent with the DFT calculations, where there are three nearly isotropic pockets labeled $\alpha$, $\beta$, and $\gamma$. We extracted the quantum oscillation frequencies of $F_\alpha = 110\,\mathrm{T}$, $F_\beta = 180\,\mathrm{T}$, and $F_\gamma = 1650\,\mathrm{T}$ at an angle $\theta$ (between the principal axis, while rotating from [100] to [110], and $B$) = 25°. We point out that the DFT calculations overestimate the size of the $\gamma$ pocket while underestimating the size of the $\alpha$ pocket in PbPd$_3$ [Fig. 5(c)]. A close inspection revealing low frequencies for the flux-grown specimen is shown in the Supplemental Material (Fig. S2) [16]. For SnPd$_3$, we extracted $F_\alpha = 170\,\mathrm{T}$ and $F_\gamma = 2500\,\mathrm{T}$ at $\theta = 30^\circ$. In this case the DFT calculations agree well with the experimental results in both the size and topography of the Fermi surfaces [Fig. 5(d)].

According to the Lifshiz-Kosevich (LK) formula [18], the temperature and the field dependencies of the oscillation amplitudes are described by the product of the thermal damping factor, $R_T = \alpha T m^*/B \sinh(\alpha T m^*/B)$ and the Dingle damping factor $R_D = \exp(-\alpha T_D m^*/B)$, where $m^*$ is the quasiparticle effective mass and $T_D$ is the Dingle temperature ($T_D = \hbar/2\pi k_B \tau_s$). One can further evaluate the scattering time $\tau_s$ and $\alpha = 2\pi^2 k_B m_e/e\hbar \approx 14.69\,\mathrm{T/K}$ with a carrier mobility $\mu_q = e\tau q/m^*$. By fitting the amplitude of the FFT peaks as a function of the temperature to the thermal damping factor, we extracted the carrier effective masses $m^*$, as shown in Fig. 6. Specifically, we obtained $m^*_\alpha = 0.12\,m_o$, $m^*_\beta = 0.09\,m_o$, and $m^*_\gamma = 0.38\,m_o$ for PbPd$_3$, and $m^*_\alpha = 0.16\ m_o$ and $m^*_\gamma = 0.75\ m_o$ for SnPd$_3$. Moreover, fitting the field dependence of the amplitude of the quantum oscillations yields $T_D(\alpha) = 25\,\mathrm{K}$ with $\mu_\alpha = 713\,\mathrm{cm^2\,V^{-1}\,s^{-1}}$, and $T_D(\gamma) = 42\,\mathrm{K}$ with $\mu_\gamma = 134\,\mathrm{cm^2\,V^{-1}\,s^{-1}}$ for PbPd$_3$, while $T_D(\alpha) = 53\,\mathrm{K}$ with $\mu_\alpha = 252\,\mathrm{cm^2\,V^{-1}\,s^{-1}}$, and $T_D(\gamma) = 10.6\ \mathrm{K}$ with $\mu_\gamma = 270\,\mathrm{cm^2\,V^{-1}\,s^{-1}}$ for SnPd$_3$.

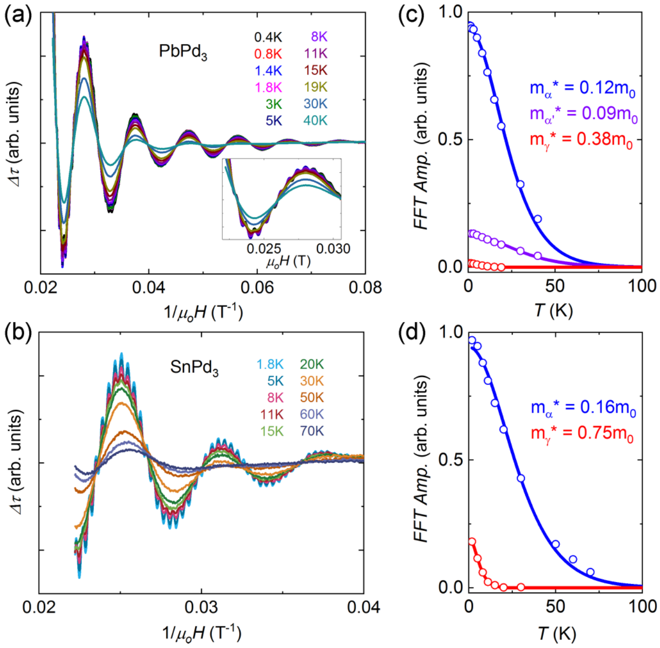

FIG. 6. (a) Background subtracted torque $\Delta\tau$ for PbPd$_3$ showing dHvA oscillations at $\theta = 14^\circ$ and at various temperatures. Inset: dHvA signal in a limited magnetic field range; i.e., $\mu_0 H = 30$–$45\,\mathrm{T}$. (b) $\Delta\tau$ for SnPd$_3$ at $\theta = 14^\circ$ at various temperatures. Amplitudes of the main peaks observed in the fast Fourier transforms (FFT) spectra of the dHvA signal as a function of temperature are shown for (c) PbPd$_3$ and (d) SnPd$_3$, respectively. Solid lines are fits to the Lifshitz-Kosevich formula [18] yielding the carrier effective masses.

Corroborated with the measured Seebeck coefficient, our Fermi surface mapping, through torque magnetometry measurements, reveals that $E_F$ is about 54 and 68 meV above the flat bands for PbPd$_3$ and SnPd$_3$, respectively. $E_F$ tuning is therefore essential in order to access the flat band to observe their contributions to the physical properties. The contributions of Pb and Pd orbitals to the band structure of PbPd$_3$ (Fig. S3 in the Supplemental Material [16]) indicate that the flat band is mainly formed by the Pd 4$d$ bands. Therefore, monovalent doping on the Pb/Sn site is expected to lower the $E_F$ while maintaining the dispersion of the flat band. In order to study the surface state, on the other hand, $E_F$ will need to be tuned away from the flat band (tune up in energy) to escape from the dominant bulk bands. For SnPd$_3$, although $E_F$ is very close to the predicted surface state, the fact that the residual resistivity of SnPd$_3$ is higher than that of PbPd$_3$ (Fig. S1 in the Supplemental Material [16]) suggests either the absence of topologically protected surface states in $\mathrm{SnPd_3}$ or that the measured transport properties are completely dominated by the bulk state. To clarify this point, careful transport studies attempting to disentangle the contribution of the bulk state and that of the surface state of this material to its electrical conduction are required. Notice that the experimentally determined position of $E_\mathrm{F}$ for $\mathrm{SnPd_3}$ implies that one should already have topological and linearly dispersing states on its surface [Fig. 4(b)], making this compound ideal for such a study.

In summary, large single crystals of $A\mathrm{Pd_3}$ ($A$ = Pb, Sn) were grown by the Czochralski technique, and $\mathrm{PbPd_3}$ was also grown by the molten flux method. The measured Seebeck coefficient suggests that the $E_\mathrm{F}$ is located above their flat bands. We further studied the geometry of the Fermi surfaces for both compounds through the dHvA effect. The topography of the Fermi surface revealed by the dHvA oscillations (under fields up to 45 T) suggest that the position of $E_\mathrm{F}$ for both compounds is at a higher energy than the values calculated by DFT, namely, 54 meV higher for $\mathrm{PbPd_3}$ and 68 meV higher for $\mathrm{SnPd_3}$. As the flat-band feature is mainly contributed by the 4*d* bands of Pd, we propose that monovalent dopants on the Pb/Sn site will lower the $E_\mathrm{F}$ and potentially provide access to the flat band. Furthermore, our experimental $E_\mathrm{F}$ suggests that in addition to the flat band in the bulk state, the Fermi arc and the Dirac surface states of $\mathrm{SnPd_3}$ should be already accessible to angle-resolved photoemission spectroscopy.

The National High Magnetic Field Laboratory is supported by National Science Foundation through Award No. NSF/DMR-1644779 and the State of Florida. K.W. acknowledges the support of the Jack E. Crow Postdoctoral Fellowship. K.-W.C. was partially supported by the NHMFL-UCGP program. J.N.N. acknowledges support from the National Science Foundation under Award No. NSF/DMR-1606952, T.S. under Award No. NSF/DMR-1534818, and G.S.N. under Award No. NSF/DMR-1748188. L.B. is supported by the Department of Energy, Basic Energy Sciences program through Award No. DE-SC0002613.

The data that support the findings of this study are available from the corresponding author upon a reasonable request.

K.W. and K.-W.C. contributed equally to this work.

---

[1] K.-H. Ahn, W. E. Pickett, and K.-W. Lee, Phys. Rev. B **98**, 035130 (2018).

[2] N. P. Armitage, E. J. Mele, and A. Vishwanath, Rev. Mod. Phys. **90**, 015001 (2018).

[3] B. Yan and C. Felser, Annu. Rev. Condens. Matter Phys. **8**, 337 (2017).

[4] Z. K. Liu, B. Zhou, Y. Zhang, Z. J. Wang, H. M. Weng, D. Prabhakaran, S.-K. Mo, Z. X. Shen, Z. Fang, X. Dai, Z. Hussain, and Y. L. Chen, Science **343**, 864 (2014).

[5] E. Tang and L. Fu, Nat. Phys. **10**, 964 (2014).

[6] V. J. Kauppila, F. Aikebaier, and T. T. Heikkilä, Phys. Rev. B **93**, 214505 (2016).

[7] P. Ravindran, P. Vajeeston, R. Vidya, A. Kjekshus, and H. Fjellvåg, Phys. Rev. B **64**, 224509 (2001).

[8] K. Mori, H. Sakakibara, H. Usui, and K. Kuroki, Phys. Rev. B **88**, 075141 (2013).

[9] Z. Zhang and J. T. Yates, Jr., Chem. Rev. **112**, 5520 (2012).

[10] W. G. Zeier, J. Schmitt, G. Hautier, U. Aydemir, Z. M. Gibbs, C. Felser, and G. J. Snyder, Nat. Rev. Mater. **1**, 16032 (2016).

[11] N. J. Ghimire, Mojammel A. Khan, A. S. Botana, J. S. Jiang, and J. F. Mitchell, Phys. Rev. Mater. **2**, 081201(R) (2018).

[12] J. Martin and G. S. Nolas, Rev. Sci. Instrum. **87**, 015105 (2016).

[13] K. Schwarz, P. Blaha, and G. Madsen, Comput. Phys. Commun. **147**, 71 (2002).

[14] J. P. Perdew, K. Burke, and M. Ernzerhof, Phys. Rev. Lett. **77**, 3865 (1996).

[15] P. M. C. Rourke and S. R. Julian, Comput. Phys. Commun. **183**, 324 (2012).

[16] See Supplemental Material at http://link.aps.org/supplemental/10.1103/PhysRevMaterials.3.041201 for other thermoelectric properties, low frequencies for the flux-grown $\mathrm{PbPd_3}$, and the contributions of Pb and Pd orbitals to the band structure of $\mathrm{PbPd_3}$.

[17] G. S. Nolas, J. W. Sharp, and H. J. Goldsmid, *Thermoelectrics: Basics Principles and New Materials Developments* (Springer-Verlag, Berlin, 2001).

[18] D. Shoenberg, *Magnetic Oscillations in Metals* (Cambridge University Press, Cambridge, 2011).